Journal of Energy Chemistry xxx (xxxx) xxx

Contents lists available at ScienceDirect

Journal of Energy Chemistry

journal homepage: www.elsevier.com/locate/jechem

http://www.journals.elsevier.com/journal-of-energy-chemistry/

MoS_2 on topological insulator Bi_2Te_3 thin films: Activation of the basal plane for hydrogen reduction

Guowei Li [a,1,*], Jue Huang [b,1], Qun Yang [a], Liguo Zhang [a], Qingge Mu [a], Yan Sun [a], Stuart Parkin [b], Kai Chang [c,*], Claudia Felser [a,*]

[a] Max Planck Institute for Chemical Physics of Solids, 01187 Dresden, Germany
[b] Max Planck Institute for Microstructure Physics, 06120 Halle, Germany
[c] Beijing Academy of Quantum Information Sciences, 100193 Beijing, China

ARTICLE INFO

Article history:
Received 27 January 2021
Revised 15 March 2021
Accepted 5 April 2021
Available online xxxx

Keywords:
MoS_2
Topological insulator
Hydrogen evolution
Surface states
Electron transfer

ABSTRACT

2H-MoS_2 is a well-studied and promising non-noble metal electrocatalyst for heterogeneous reactions, such as the hydrogen evolution reaction (HER). The performance is largely limited by the chemically inert basal plane, which is unfavorable for surface adsorption and reactions. Herein, we report a facile method to boost the HER activities of 2H-MoS_2 by coupling with epitaxial Bi_2Te_3 topological insulator films. The as-obtained MoS_2/ Bi_2Te_3/$SrTiO_3$ catalyst exhibits prominent HER catalytic activities compared to that of pure MoS_2 structures, with a 189 mV decrease in the overpotential required to reach a current density of 10 mA cm^{-2} and a low Tafel slope of 58 mV dec^{-1}. Theoretical investigations suggest that the enhanced catalytic activity originates from the charge redistribution at the interface between the Bi_2Te_3topological insulator films and the MoS_2 layer. The delocalized *sp*-derived topological surface states could denote electrons to the MoS_2 layer and activate the basal plane for hydrogen adsorption. This study demonstrates the potential of manipulating topological surface states to design high-performance electrocatalysts.

1. Introduction

Emerging topological materials provide an ideal platform to explore the relationship between exotic topological properties and surface chemical reactions. Benefiting from symmetry-protected topological orders, topological materials exhibit distinctively different behaviors compared to those of topologically trivial materials, from robust topological surface states (TSSs) to high-mobility carriers [1]. Acceptor- or donor-like TSSs are active for the adsorption of reaction intermediates and can act as electron baths for reduction or oxidation reactions [2,3]. As the existence of a TSS is protected by the bulk band structure, they cannot be eliminated by surface defects, dangling bonds, or molecular adsorption [4,5]. These properties have evoked a wave of research interest to understand and design topological phase catalysts for heterogeneous reactions such as hydrogen evolution reactions (HERs).

Topological insulators (TIs) in the Bi_2Se_3 family, such as Bi_2Se_3 and Bi_2Te_3, are commonly believed to be model topological insulator systems with a well-defined bulk bandgap and a single-Dirac-cone surface state, which are ideal for studying the role of TSSs in catalytic reactions [6–8]. Early theoretical investigations indicate that the adsorption energies of small molecules such as CO and O_2 can be enhanced due to the delocalized surface states when Bi_2Se_3 thin films are used as substrates [9]. This strategy has proved effective in tailoring the adsorption behavior of other transition metals, including Au, Ag, Cu, Pt, and Pd [10]. However, topological Bi_2Se_3-family compounds themselves are not suitable as HER catalysts. The *sp*-like TSSs result in weak bonding between the HER intermediates and catalyst surfaces, leading to a slow Volmer process because of the low coverage of the reaction intermediates [11]. Even when using Bi_2Se_3 and Bi_2Te_3 nanostructures, an extremely high overpotential of above 600 mV is needed to deliver a current density of 10 mA cm^{-2} [12]. Thus, it remains a challenge to combine the advantages of robust TSSs and favorable Gibbs free energy in the design of high-performance HER catalysts.

Coupling topological materials with transition-metal-based compounds has been considered an effective strategy to address the problems mentioned above. The vertical position of the TSSs

* Corresponding authors.
E-mail addresses: guowei.li@cpfs.mpg.de (G. Li), changkai@baqis.ac.cn (K. Chang), claudia.felser@cpfs.mpg.de (C. Felser).
[1] These authors contributed equally.

https://doi.org/10.1016/j.jechem.2021.04.010

can be adjusted by depositing a conventional insulator overlayer onto a TI substrate due to topological proximity effects [13]. In other words, the TSSs can float onto the top of the conventional insulator layer, suggesting the possibility of tailoring the surface catalysis behavior. This theory was verified by constructing monolayer ZnSe on Bi_2Se_3 films, resulting in favorable Gibbs free energy for the HER [14]. The enhanced HER performance is ascribed to the decrease in the band gap, as well as the low surface resistivity resulting from the metallic TSSs [15]. However, most of the reported experimental works have focused on the design of nanocomposites with uncertain exposed crystal surfaces and unexpected defects, causing difficulties in precisely understanding the contribution of TSSs [16–18].

To overcome the problem of an uncertain crystal structure, we constructed a new heterostructure with well-defined, chemically stoichiometric compositions and atomically shaped interfaces. First, high-quality stoichiometric single-crystalline Bi_2Te_3 films with determined crystal surfaces were used as the substrates. Next, 2H-MoS_2 thin layers, with their HER mechanism having been unambiguously determined, were deposited on the Bi_2Te_3 films [19–22]. Our experimental results indicate that the MoS_2/Bi_2Te_3 heterostructure exhibits a lower overpotential and Tafel slope than those of pure MoS_2 nanostructures. In situ scanning electrochemical microscopy (SECM) revealed high HER kinetics in the presence of Bi_2Te_3 films. In combination with density functional theory calculations, it was found that the originally inert basal plane of MoS_2 can be activated due to charge redistribution in the MoS_2 layer as a result of electron transfer from the *p* orbitals of TSSs. This study provides an alternative strategy to utilize the large area of the basal plane for MoS_2, although they are still not as active as the edges [23,24].

2. Experimental

2.1. Synthesis of Bi_2Te_3 topological insulator thin films

The Bi_2Te_3 films were grown on niobium-doped $SrTiO_3$(111) (STO) substrates in an ultra-high vacuum molecular beam epitaxy (MBE) system with a base pressure of $\sim 8 \times 10^{-11}$ mbar. High-purity Bi (99.9999%) and Te (99.9999%) were evaporated from separated standard Knudsen cells. The critical growth parameters were the flux ratio of Te_2/Bi (θ) and substrate temperature (T_{sub}). The conditions for layer-by-layer growth of Bi_2Te_3 films were established with θ maintained at approximately 15–20 and T_{sub} set at approximately 115 °C.

2.2. Synthesis and exfoliation of MoS_2 nanostructures

$(NH_4)_2MoS_4$ (50 mg) was placed in a 30 mL autoclave filled with 20 mL of N, N-dimethylformamide. $N_2H_4{\cdot}H_2O$ (0.1 mL) was added dropwise. The mixed solution was transferred into an oven and heated at 180 °C for 24 h. The resulting product was washed with water, then with ethanol, and dried at 60 °C. For the exfoliation process, the as-prepared bulk MoS_2 precursor was added to a 50 mL glass vial containing 30 mL of N, N-dimethylformamide. The mixtures were sonicated in a water-cooled bath at 25 °C for 12 h and then centrifuged at 6000 rpm for 10 min to remove the residual bulk MoS_2. The suspensions were dried and re-dispersed in ethanol for the following drop-casting process.

2.3. Synthesis of MoS_2/Bi_2Te_3 nanostructured catalysts

Bi_2Te_3 nanoplates were synthesized first with a solvothermal method. 0.4 g of polyvinylpyrrolidone, 0.32 g of NaOH, 0.45 g of $Bi(NO_3)_3{\cdot}xH_2O$, and 0.4 g of $NaTeO_3$ were placed in a beaker and filled with 30 mL of ethylene glycol. The precursor solution was stirred for 5 h and then sealed in the autoclave and heated at 180 °C for 24 h. The residue was washed thoroughly and then dried under vacuum at 60 °C for 24 h. For the deposition of MoS_2 nanoparticles, 50 mg of the Bi_2Te_3 nanoplates and 10 mg of $(NH_4)_2$-MoS_4 were mixed. This experimental procedure is the same as the description in section 2.2.

2.4. Materials characterization

The film deposition was monitored by *in situ* reflection high-energy electron diffraction (RHEED), and *ex-situ* X-ray diffraction (XRD, Brucker D8), and atomic force microscopy (AFM). The surface morphology of the film of MoS_2 nanoparticles was recorded using a TESCAN scanning electron microscope. Raman spectra were recorded using a customary confocal micro-Raman spectrometer with a HeNe-laser (wavelength 632 nm) as the excitation source and a single-grating spectrograph with 1 cm^{-1} resolution.

2.5. Electrochemical measurements

The electrochemical performance was assessed in a 0.5 M H_2SO_4 electrolyte on an Autolab PGSTAT302N with a conventional three-electrode cell configuration. The MoS_2 ink was drop-cast on the required substrate (STO or Bi_2Te_3/STO) and simultaneously baked to evaporate the solvent. Substrates with different catalysts were attached to a Ti wire and used directly as a working electrode. An Ag/AgCl (3 M KCl) electrode was used as the reference electrode, and a graphite rod was used as the counter electrode. Linear sweep voltammetry was performed at a scan rate of 1 mV/s. All of the polarization curves were IR-corrected using electrochemical impedance spectroscopy (EIS). All of the potentials reported in this work were converted to the reversible hydrogen electrode potential according to E (versus RHE) = E (versus Ag/AgCl) + (0.207 + 0.059 pH) V.

SECM was carried out using an SECM setup (Sensolytics, Bochum, Germany) in combination with an Autolab PGSTAT302N potentiostat. The electrochemical cell was composed of four electrodes. A Pt wire with a diameter of 10 μm sealed in a soda-lime glass served as working electrode 1. A Pt mesh was used as the counter electrode, and Ag/AgCl (3 M KCl) in the aqueous phase was used as the reference electrode. The studied catalyst on the substrate acted as working electrode 2.

3. Results and discussion

3.1. Structure characterization of topological thin films and 2H– MoS_2

The final device (MoS_2/Bi_2Te_3/STO) used for the electrocatalytic HER assessment is illustrated in Fig. 1a. First, high-quality Bi_2Te_3 single-crystalline films were grown on conductive Nb-doped STO substrates by MBE, with the method optimized based on a previous study [25]. The surface morphology and roughness were characterized by AFM. It is interesting to observe that the films exhibited flat surfaces at a large scale with atomically flat terraces, indicating high-quality thin films (Fig. 1b and Fig. S1). The atomically flat morphology was further confirmed by the sharp streaky pattern resulting from RHEED under electron incidence in the $11\bar{2}$ direction (Fig. 1c). A lattice spacing of 4.38 Å is indicated by the corresponding principal diffraction lines, which is consistent with rhombohedral Bi_2Te_3. The phase and crystallinity of the films were identified by XRD (Fig. 1d). Only diffraction peaks belonging to the (003) family are observed in the θ–2θ scan, indicating preferential c-axis-oriented epitaxial growth of the Bi_2Te_3 films along the [111] plane of the $SrTiO_3$ substrate. Bulk MoS_2 thin films were deposited

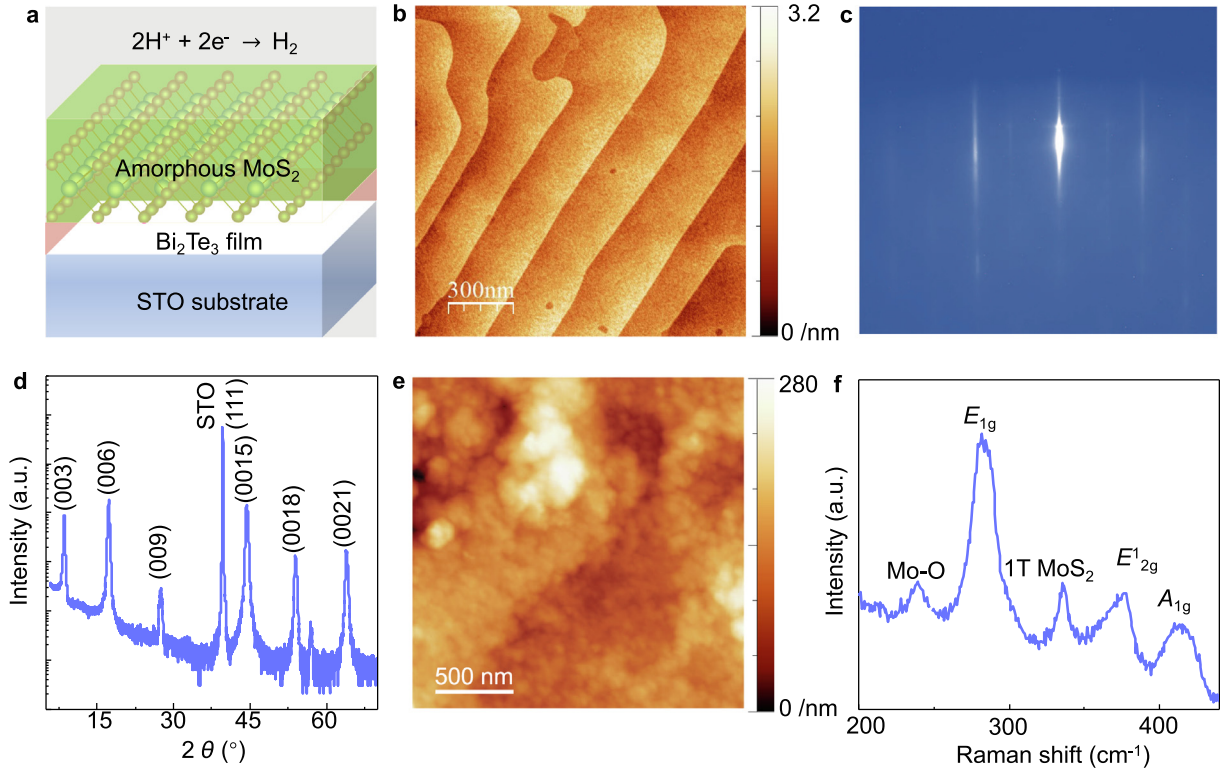

Fig. 1. (a) Illustration of the MoS_2/Bi_2Te_3/STO heterostructure catalysts. (b). AFM surface morphology of Bi_2Te_3 films grown on STO substrate, and (c) the corresponding RHEED pattern. (d) XRD scan of the as-prepared single-crystalline Bi_2Te_3 films. (e) AFM image of the drop-casted MoS_2 thin layer on Bi_2Te_3 films. (f) Raman spectroscopy of the exfoliated MoS_2 thin layer.

on the as-prepared Bi_2Te_3/STO substrate using a drop-casting method [26]. As revealed by the AFM image (Fig. 1e), the liquid-exfoliated MoS_2 nanoparticles were uniformly distributed with an average film thickness of ~ 100 nm on the top of the Bi_2Te_3 layer. The crystal structure of the exfoliated MoS_2 nanoparticles was characterized by Raman spectroscopy (Fig. 1f). The Raman shifts (283, 377, and 414 cm^{-1}) are associated with the phonon modes of E_{1g}, E^1_{2g}, and A_{1g} in 2H-MoS_2, respectively [27,28]. The peak at 336 cm^{-1} suggests the existence of a small amount of 1 T-MoS_2 [29]. Minor surface oxidation was observed from Mo–O stretching frequencies at 240 cm^{-1}. The successful deposition was further confirmed by energy-dispersive X-ray spectroscopy, in which Mo, S, Bi, and Te were detected (Fig. S2).

3.2. Electrochemical HER performance of MoS_2 based catalysts

The experiments were conducted in an Ar-saturated 0.5 M H_2SO_4 electrolyte solution using a standard three-electrode electrochemical setup with a graphite rod as the counter electrode. The device was attached to a Ti wire and served as the working electrode. For a clear understanding of the role of topological thin films, several other devices, including a pure substrate (STO), MoS_2-deposited STO without TI films (MoS_2/STO), and TI films without MoS_2 layers (Bi_2Te_3/STO) were also investigated. As shown by the *i*R corrected polarization curves in Fig. 2a, the STO substrate and Bi_2Te_3 thin films have negligible activities in the HER. This is consistent with previous research stating that, even with exfoliated Bi_2Te_3 few-layered nanosheets, an overpotential of nearly 700 mV is needed to deliver a current density of 10 mA cm^{-2} [12].

The slow reaction kinetics are a result of the extremely weak hydrogen adsorption at the Bi_2Te_3 (001) surface (0.8 eV), leading to a low reaction intermediate coverage [11]. The direct deposition of exfoliated MoS_2 nanoparticles onto the STO substrate (MoS_2/STO) led to an enhanced HER efficiency with an overpotential of 437 mV to reach the same current density, which is consistent with previous research on various MoS_2 films [30]. Thus, it was concluded that Bi_2Te_3 thin films and exfoliated pristine MoS_2 nanosheets are not active in the HER. In sharp contrast, an overpotential of only 248 mV was required to reach a current density of 10 mA cm^{-2} when a layer of Bi_2Te_3 thin film was introduced between the MoS_2 nanosheets and STO substrate (MoS_2/Bi_2Te_3/STO). It should be pointed out that the use of high-quality epitaxial thin films is not necessary, as the interaction of 2H MoS_2 (001) surface and Bi_2Te_3 (001) surface is pretty strong with an adsorption energy of −1.7 eV. We expect a similar enhancement catalytic activity with Bi_2Te_3 nanostructures. Thus, MoS_2/Bi_2Te_3 nanostructured catalysts were synthesized successfully as evidenced by the SEM images, XRD diffraction, and element analysis (Fig. S3). The drop-casted MoS_2/Bi_2Te_3 nanostructured on STO exhibited displayed a similar HER activity with the thin film's system (Fig. S4). The overpotential decreased to only 160 mV at a current density of 10 mA cm^{-2} and shows high stability when deposited on the more conductive Ni foam (Fig. 2a, Fig. S5). This overpotential places the modified thin films in the top tier of MoX_2 (X = S, Se)-based hydrogen evolution catalysts [21,31] and better than the recently reported topological Bi_2X_3 (X = Se, Te) catalysts (Table S1) [11,32,33].

The enhanced catalytic performances were confirmed kinetically from the Tafel slopes derived from the polarization curves of the three samples (Fig. 2b). An extremely high Tafel slope of 168 mV dec^{-1} was observed for the Bi_2Te_3 thin film catalyst, which is consistent with the poor HER activity. The Tafel slope of the MoS_2 nanosheet catalyst has a two-step characteristic, starting from 80 mV dec^{-1} at the low overpotential range and shifting to as high as 361 mV dec^{-1} at potentials above 380 mV. Similar results were observed for a state-of-the-art Pt/C catalyst, with

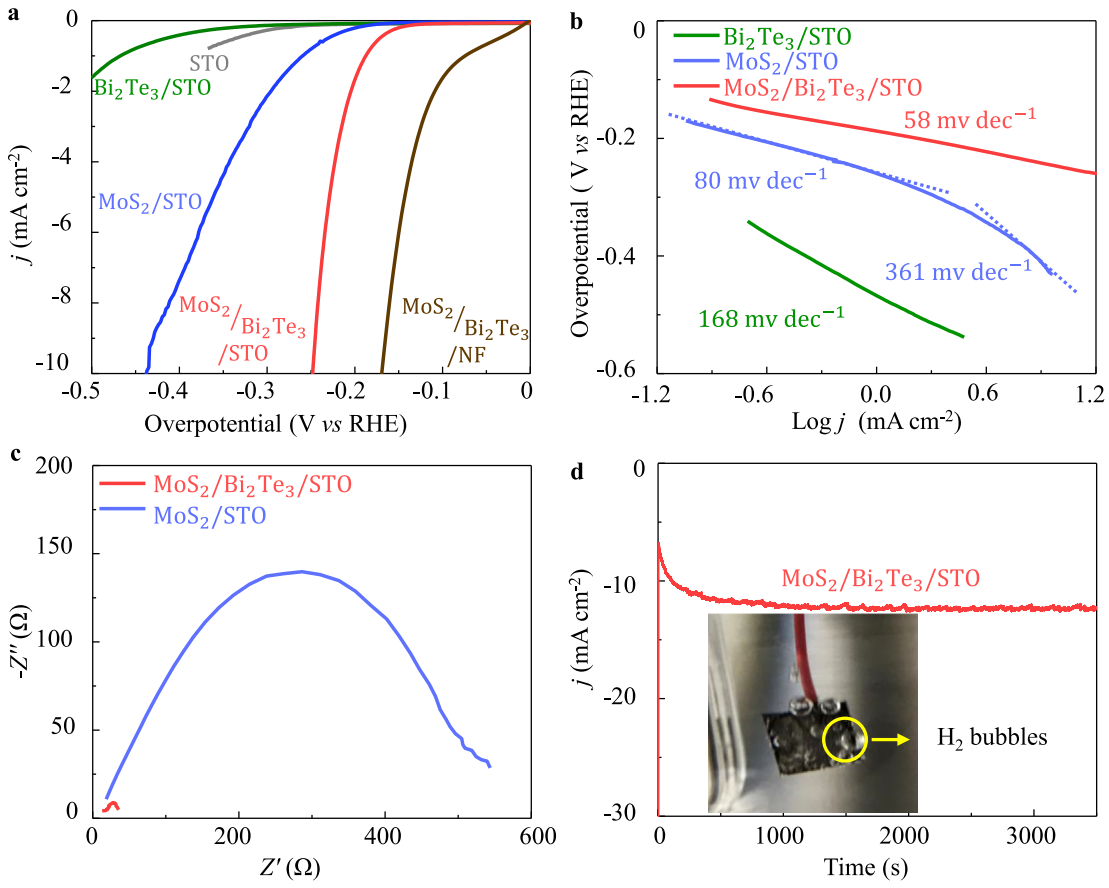

Fig. 2. (a) HER polarization curves of the pure STO substrate, MoS_2/STO, Bi_2Te_3/STO, and MoS_2/Bi_2Te_3/STO catalysts. (b) Corresponding Tafel plots were obtained from the polarization curves. (c) Nyquist plots of MoS_2/STO and MoS_2/Bi_2Te_3/STO catalysts. (d) Stability test of the MoS_2/Bi_2Te_3/STO heterostructure catalysts; inset: the electrolytic evolution of hydrogen bubbles at the catalyst surface.

the Tafel slope shifting from 30 to 120 mV dec^{-1} as the overpotential increased, indicating that the reaction kinetics and mechanisms are strong potential and coverage dependent [34,35]. However, the Tafel slope of the MoS_2/Bi_2Te_3/STO catalysts was significantly lower at 58 mV dec^{-1}, which compares favorably with other recently reported high-performance earth-abundant HER electrocatalysts [36]. Impressively, there is no transition in the Tafel slopes over a wide overpotential range, suggesting high stability of the rate constant even at a high intermediate species coverage [37]. To better understand the role of Bi_2Te_3 thin films on the boosted HER activity of MoS_2, EIS analyses of the two electrodes with and without the Bi_2Te_3 interlayer were performed under the same conditions (Fig. 2c). The Nyquist plots show that MoS_2/Bi_2Te_3/STO catalysts have a much smaller charge transfer resistance than bare MoS_2, indicating a faster Faradaic process and better HER kinetics with the introduction of a Bi_2Te_3 thin film layer. As another important criterion for HER catalysts, the long-term electrocatalytic stability of the MoS_2/Bi_2Te_3/STO catalyst was determined by the constant current–time curve, with a clear hydrogen bubble forming at the surface (Fig. 2d).

3.3. In-situ SECM investigation of HER performance

To spatially probe the difference in catalytic activities with and without the Bi_2Te_3 interlayer, SECM was used to map the local electron transfer kinetics. MoS_2 nanosheets were deposited on an STO substrate half-covered with Bi_2Te_3 thin films. This served as working electrode 2, as illustrated in Fig. 3a. A Pt wire with a diameter of 10 μm was sealed in soda-lime glass and served as a working electrode for current collection. Ag/AgCl (3 M KCl) in the aqueous phase was used as the reference electrode. The approach curve was constructed with the feedback model in a solution of 5 mM $[Fe(CN)_6]^{3-}$ in 100 mM KCl (Fig. S6). The tip current (*it*)-distance curve exhibited a typical SECM negative feedback model, indicating a low conductivity of the semi-conductive 2H phase MoS_2. The HER activities of the catalysts with and without the Bi_2Te interlayer thin films were detected using the substrate generation/tip collection (SG/TC) mode. An $HClO_4$ electrolyte with a concentration of 100 mM was used for stable tip current collection. Fig. 3b depicts CVs performed at different positions and clearly shows that the MoS_2/Bi_2Te_3/STO catalysts have higher activities than those without the Bi_2Te_3 interlayer. The HER catalytic activity maps of the catalysts at a constant applied potential are displayed in Fig. 3c. Low activity was observed in areas without the Bi_2Te interlayer, and activity increased rapidly when the tip was moved to the top of the MoS_2/Bi_2Te_3/STO catalyst. The corresponding line profile extracted from the SG/TC mode provides an intuitive view of the differences in HER activity. The HER activity increased three-fold in the presence of the Bi_2Te_3 interlayer (Fig. 3d).

3.4. Theoretical understanding of the role of TI substrate

TIs such as those in the Bi_2Se_3 family have unfilled TSSs around the Fermi level, which is derived from the delocalized *sp*-band. They could donate or accept electrons for the surface adsorbates and tailor the adsorption energy [9]. To probe the role of the Bi_2Te_3 interlayer in the HER catalytic process, a three-dimensional charge density difference simulation for the heterostructure catalysts was

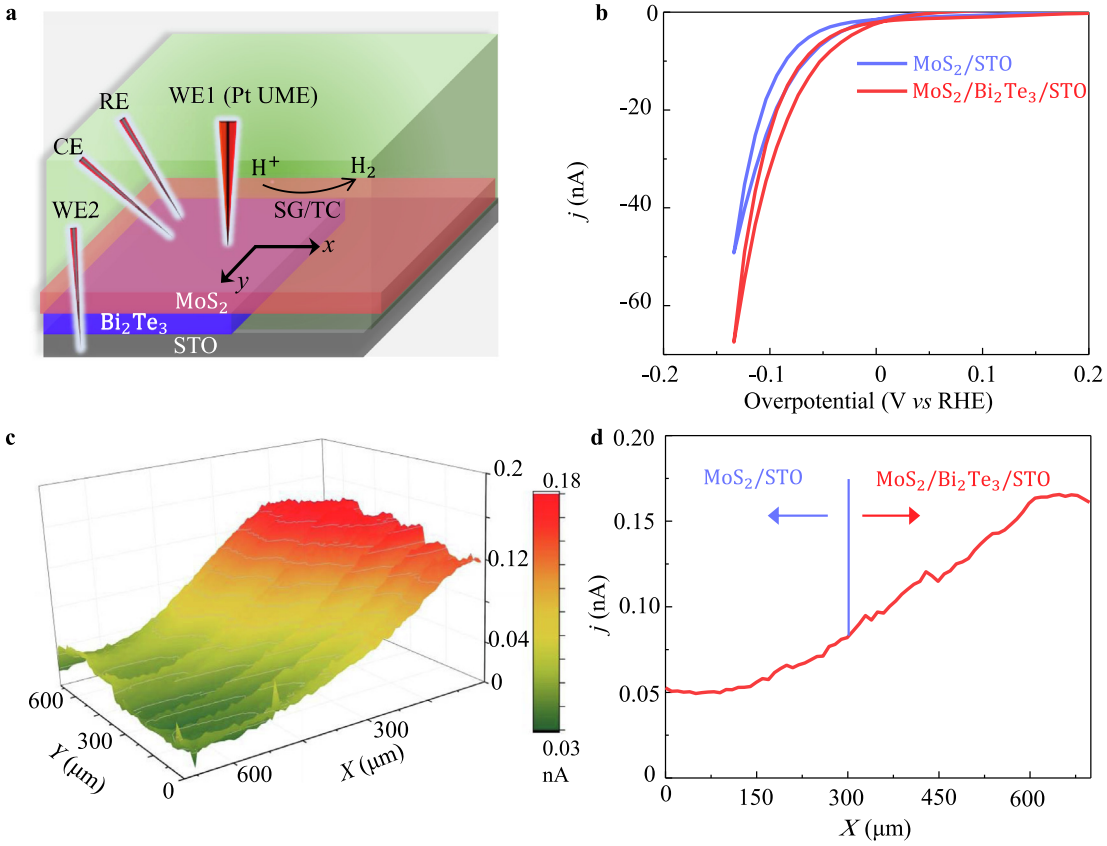

Fig. 3. (a) Schematic representation of the setup for SECM measurements. (b) CV curves were obtained with the tip on the position of MoS_2/STO and MoS_2/Bi_2Te_3/STO areas. (c) SG/TC mode (HER activity) image of the catalysts containing MoS_2/STO and MoS_2/Bi_2Te_3/STO. (d) HER SG/TC line profile with the tip scanned from MoS_2/STO to MoS_2/Bi_2Te_3/STO area.

carried out. It can be seen clearly that charge redistribution mainly occurs near the interfacial region between MoS_2 and the Bi_2Te_3 substrate (Fig. 4a). More specifically, charge accumulation

occurs in the central region of the interface, while the charge depletion is mostly distributed on the topological Bi_2Te_3 substrate, suggesting charge transfer to the MoS_2

layer. This is important for tailoring the adsorption energy of the MoS_2 basal plane, which is well agreed to be catalytically inert toward adsorption and catalysis. To further elucidate the influence of charge redistribution on the HER, we considered the adsorption of hydrogen on the MoS_2 basal plane. The electron depletion region occurs mainly around the S atoms, suggesting their tendency to donate electrons to the adsorbed H atom. At the same time, clear charge accumulation was observed between the S atoms and the adsorbed H atom. Bader charge analysis revealed an electron loss of 0.04 from the MoS_2 monolayer, indicating better adsorption of hydrogen at the basal plane (Fig. 4b). The electron re-distribution in the interface is further evidenced by the Raman spectroscopy recorded on pure Bi_2Se_3 and MoS_2/Bi_2Se_3 hybrid (Fig. 4c). Four Raman active modes were observed for pure Bi_2Se_3, which is consistent with the literature [38]. However, with MoS_2 loaded, the intensity of A_u^1 peak decreased significantly. This suggests an increase in electron density and lowered energy at atoms on the surface, which making the vibration weak out of the plane and thus Raman inactive [38,39]. The Gibbs free energy of hydrogen adsorption decreased from 2.43 eV for the basal plane to 1.4 eV for the MoS_2/Bi_2Te_3/STO heterostructures, although it is still inferior to the edges of the MoS_2 catalyst (Fig. 4d). These theoretical investigations suggest the importance of the Bi_2Te_3 layer. The *sp*-band-derived topological non-trivial surface states of Bi_2Te_3 could deliver electrons to the surface adsorbates even when they are covered with a thin layer of topological trivial thin films [14]. Such an electron transfer process is accompanied by a position shift of the Dirac points associated with the topological non-trivial surface states, but they will not be destroyed due to the bulk band protection (Fig. 4e). The electron redistribution leads to electron depletion at the S atoms, especially at the surface layer of the MoS_2 basal plane (Fig. 4c). Correspondingly, there is an upward shift of the *p*-band center with respect to the Fermi energy, which enhances the binding energy of the H atom at the S sites (Fig. 4f) [40].

4. Conclusions

In summary, we explored the role of topological non-trivial surface states in the surface reactivity of HER catalysts. The introduction of the topological Bi_2Te_3 layer enhanced the activity exhibited by the inert basal plane of MoS_2 toward hydrogen evolution. The formation of MoS_2/Bi_2Te_3/STO heterostructures resulted in significant charge redistribution in the interface. The *sp*-derived surface states could donate electrons to the MoS_2 layer and reshape the *p*-band orbitals of the surface S atoms. This leads to an upshift of the *p*-band center and an increased H binding energy, which activates the originally chemically inert basal plane of MoS_2. These results are significant for the design of high-performance catalysts by manipulating topological non-trivial surface states.

Author contributions

Li G, Chang K, and Felser C supervised the project and designed the research. Li G, and Huang J contribute equally to this work.

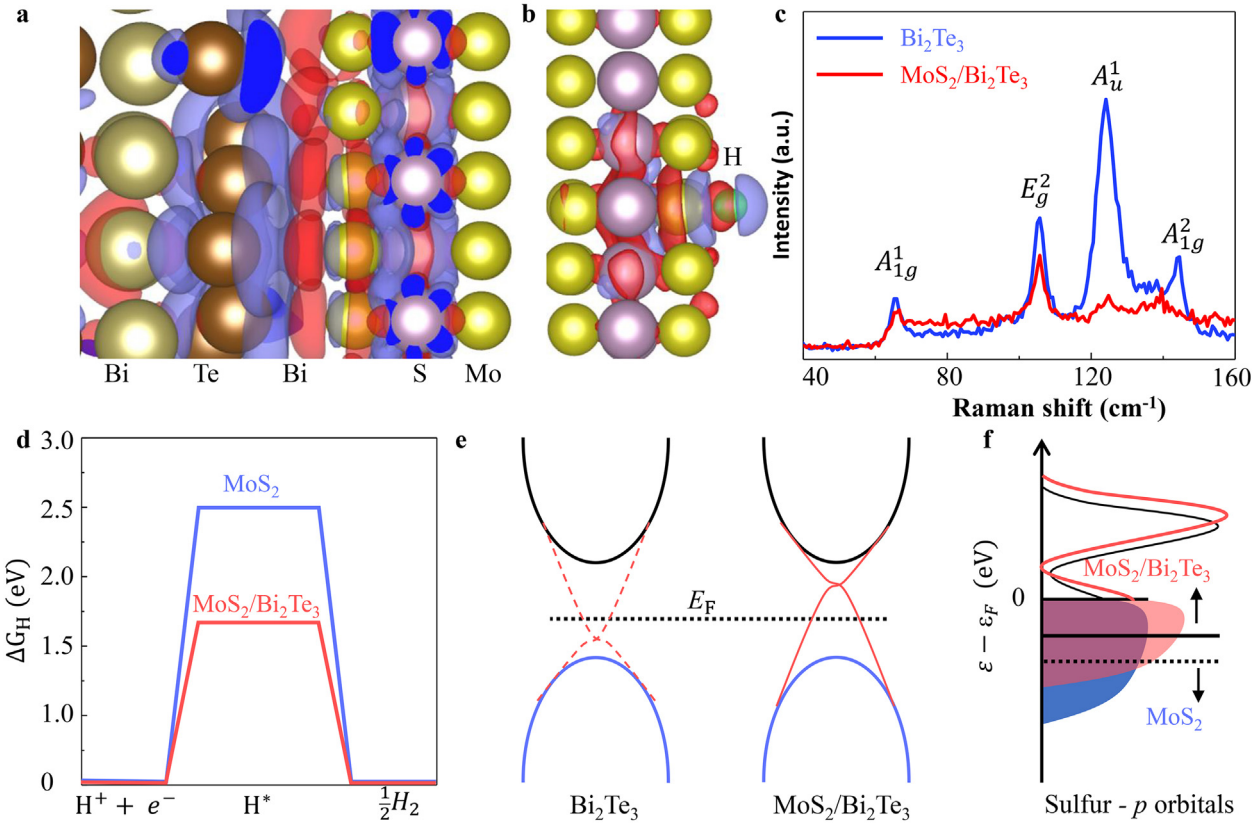

Fig. 4. Three-dimensional charge density difference for the MoS_2/Bi_2Te_3 heterostructure (a) without and (b) with H adsorption. Red and blue iso-surfaces represent charge accumulation and depletion in the space. (c) Gibbs free energy of hydrogen adsorption for the basal plane of MoS_2 and MoS_2/Bi_2Te_3 heterostructure. (d) An illustration of the changing of Dirac point regarding the TSSs of Bi_2Te_3. (e) A comparison of p band center with and without Bi_2Te_3 layer for MoS_2 catalyst.

Huang J synthesized the topological thin films and characterized them under the supervision of Chang K and Parkin S. Yang Q and Sun Y performed the theoretical calculation and analysis, Li G performed electrochemical measurements and analysis. Huang J and Zhang L carried out the AFM measurement. Mu Q measured the Raman spectroscopy. Li G wrote the paper with support from Huang J., and Chang K. All authors contributed to the general discussion.

Declaration of Competing Interest

The authors declare that they have no known competing financial interests or personal relationships that could have appeared to influence the work reported in this paper.

Acknowledgments

This work was financially supported by the European Research Council (ERC Advanced Grant No. 291472 'Idea Heusler') and the ERC Advanced Grant (No. 742068). TOPMAT'. K.C. was funded by the National Natural Science Foundation of China (Grant No. 12074038). J. H. and S. P. were supported by the Deutsche Forschungsgemeinschaft (DFG, German Research Foundation) No. 314790414.

Appendix A. Supplementary data

Supplementary data to this article can be found online at https://doi.org/10.1016/j.jechem.2021.04.010.

References

[1] C. Fu, Y. Sun, C. Felser, APL Mater. 8 (2020) 040913.
[2] G. Li, Q. Xu, W. Shi, C. Fu, L. Jiao, M.E. Kamminga, M. Yu, H. Tuysuz, N. Kumar, V. Suss, R. Saha, A.K. Srivastava, S. Wirth, G. Auffermann, J. Gooth, S. Parkin, Y. Sun, E. Liu, C. Felser, Sci. Adv. 5 (2019) eaaw9867.
[3] G. Li, C. Fu, W. Shi, L. Jiao, J. Wu, Q. Yang, R. Saha, M.E. Kamminga, A.K. Srivastava, E. Liu, A.N. Yazdani, N. Kumar, J. Zhang, G.R. Blake, X. Liu, M. Fahlman, S. Wirth, G. Auffermann, J. Gooth, S. Parkin, V. Madhavan, X. Feng, Y. Sun, C. Felser, Angew. Chem. 131 (2019) 13241–13246.
[4] L. Muchler, H. Zhang, S. Chadov, B. Yan, F. Casper, J. Kubler, S.C. Zhang, C. Felser, Angew. Chem. 51 (2012) 7221–7225.
[5] L.M. Schoop, F. Pielnhofer, B.V. Lotsch, Chem. Mater. 30 (2018) 3155–3176.
[6] X. Wang, G. Bian, T. Miller, T.C. Chiang, Phys Rev Lett 108 (2012) 096404.
[7] L. Zhang, D. Zhao, Y. Zang, Y. Yuan, G. Jiang, M. Liao, D. Zhang, K. He, X. Ma, Q. Xue, APL Mater. 5 (2017) 076106.
[8] Y.Y. Li, G. Wang, X.G. Zhu, M.H. Liu, C. Ye, X. Chen, Y.Y. Wang, K. He, L.L. Wang, X.C. Ma, H.J. Zhang, X. Dai, Z. Fang, X.C. Xie, Y. Liu, X.L. Qi, J.F. Jia, S.C. Zhang, Q.K. Xue, Adv. Mater. 22 (2010) 4002–4007.
[9] H. Chen, W. Zhu, D. Xiao, Z. Zhang, Phys. Rev. Lett. 107 (2011) 056804.
[10] J. Xiao, L. Kou, C.-Y. Yam, T. Frauenheim, B. Yan, ACS Catal. 5 (2015) 7063–7067.
[11] Q. Qu, B. Liu, J. Liang, H. Li, J. Wang, D. Pan, I.K. Sou, ACS Catal. 10 (2020) 2656–2666.
[12] A. Ambrosi, Z. Sofer, J. Luxa, M. Pumera, ACS Nano 10 (2016) 11442–11448.
[13] G. Wu, H. Chen, Y. Sun, X. Li, P. Cui, C. Franchini, J. Wang, X.Q. Chen, Z. Zhang, Sci. Rep. 3 (2013) 1233.
[14] L. Li, J. Zeng, W. Qin, P. Cui, Z. Zhang, Nano Energy 58 (2019) 40–46.
[15] K. Yin, Z.D. Cui, X.R. Zheng, X.J. Yang, S.L. Zhu, Z.Y. Li, Y.Q. Liang, J. Mater. Chem. A (2015) 22770–22780.
[16] C. Nethravathi, A. Manganahalli, M. Rajamathi, A.C.S. Appl, Nano Mater. 2 (2019) 2005–2012.
[17] R. Ma, G. Lin, Y. Zhou, Q. Liu, T. Zhang, G. Shan, M. Yang, J. Wang, npj Comput Mater. 5 (2019) 1.
[18] G. Li, B. Zhang, J. Rao, D. Herranz Gonzalez, G.R. Blake, R.A. de Groot, T.T.M. Palstra, Chem. Mater. 27 (2015) 8220–8229.
[19] G. Li, D. Zhang, Q. Qiao, Y. Yu, D. Peterson, A. Zafar, R. Kumar, S. Curtarolo, F. Hunte, S. Shannon, Y. Zhu, W. Yang, L. Cao, J. Am, Chem. Soc. 138 (2016) 16632.
[20] D. Zhao, Z. Zhuang, X. Cao, C. Zhang, Q. Peng, C. Chen, Y. Li, Chem. Soc. Rev. 49 (2020) 2215–2264.

[21] Q. Ding, B. Song, P. Xu, S. Jin, Chem. 1 (2016) 699–726.
[22] Q. Zhou, J. Feng, X. Peng, L. Zhong, R. Sun, J. Energy Chem. 45 (2020) 45–51.
[23] G. Li, C. Fu, J. Wu, J. Rao, S.-C. Liou, X. Xu, B. Shao, K. Liu, E. Liu, N. Kumar, X. Liu, M. Fahlman, J. Gooth, G. Auffermann, Y. Sun, C. Felser, B. Zhang, Appl. Catal. B 254 (2019) 1–6.
[24] D. Yang, Q. Zhu, B. Han, The Innovation 1 (2020) 100016.
[25] C.Z. Chang, K. He, L. Wang, X. Ma, M. Liu, Z. Zhang, X. Chen, Y. Wang, Q. Xue, Spin 01 (2012) 21–25.
[26] Y.K. Srivastava, A. Chaturvedi, M. Manjappa, A. Kumar, G. Dayal, C. Kloc, R. Singh, Adv. Opt. Mater. 5 (2017) 1700762.
[27] H. Fan, R. Wu, H. Liu, X. Yang, Y. Sun, C. Chen, J. Mater. Sci. 53 (2018) 10302–10312.
[28] S. Cong, X. Liu, Y. Jiang, W. Zhang, Z. Zhao, The Innovation 1 (2020) 100051.
[29] S. Shi, D. Gao, B. Xia, P. Liu, D. Xue, J. Mater. Chem. A 3 (2015) 24414–24421.
[30] G. Li, D. Zhang, Y. Yu, S. Huang, W. Yang, L. Cao, J. Am. Chem. Soc. 139 (2017) 16194–16200.
[31] C. Tang, M.-M. Titirici, Q. Zhang, J Energy Chem. 26 (2017) 1077–1093.
[32] D. Li, J. Lao, C. Jiang, Y. Shen, C. Luo, R. Qi, H. Lin, R. Huang, G.I.N. Waterhouse, H. Peng, J. Catal. 381 (2020) 590–598.
[33] J. Yang, C. Wang, H. Ju, Y. Sun, S. Xing, J. Zhu, Q. Yang, Adv. Funct. Mater. 27 (2017) 1703864.
[34] B.E. Conway, L. Bai, J. Electroanal. Chem. 198 (1986) 149–175.
[35] J. Gan, Z. Huang, W. Luo, W. Chen, Y. Cao, G. Qian, X. Zhou, X. Duan, J. Energy Chem. 52 (2021) 33–40.
[36] S. Jayabal, G. Saranya, J. Wu, Y. Liu, D. Geng, X. Meng, J. Mater. Chem. A 5 (2017) 24540–24563.
[37] T. Shinagawa, A.T. Garcia-Esparza, K. Takanabe, Sci. Rep. 5 (2015) 13801.
[38] L. Ren, X. Qi, Y. Liu, G. Hao, Z. Huang, X. Zou, L. Yang, J. Li, J. Zhong, J. Mater, Chem. 22 (2012) 4921–4926.
[39] G.B. Osterhoudt, R. Carelli, K.S. Burch, F. Katmis, N. Gedik, J.S. Moodera, Phys. Rev. B 98 (2018) 014308.
[40] C. Tsai, F. Abild-Pedersen, J.K. Norskov, Nano Lett. 14 (2014) 1381–1387.